TU Delft

Delft University of Technology

Document Version
Final published version

Licence
CC BY

Citation (APA)
Bensason, D., Sciacchitano, A., & Ferreira, C. (2024). Experimental study of the impact of blade-tip mounted rotors on the X-Rotor vertical-axis wind turbine. *Journal of Physics: Conference Series*, *2767*(7), Article 072016. https://doi.org/10.1088/1742-6596/2767/7/072016

Important note
To cite this publication, please use the final published version (if applicable).
Please check the document version above.

Copyright
In case the licence states “Dutch Copyright Act (Article 25fa)”, this publication was made available Green Open Access via the TU Delft Institutional Repository pursuant to Dutch Copyright Act (Article 25fa, the Taverne amendment). This provision does not affect copyright ownership.
Unless copyright is transferred by contract or statute, it remains with the copyright holder.

Sharing and reuse
Other than for strictly personal use, it is not permitted to download, forward or distribute the text or part of it, without the consent of the author(s) and/or copyright holder(s), unless the work is under an open content license such as Creative Commons.

Takedown policy
Please contact us and provide details if you believe this document breaches copyrights.
We will remove access to the work immediately and investigate your claim.

*This work is downloaded from Delft University of Technology.*

Journal of Physics: Conference Series

PAPER • OPEN ACCESS

# Experimental study of the impact of blade-tip mounted rotors on the X-Rotor vertical-axis wind turbine

To cite this article: David Bensason *et al* 2024 *J. Phys.: Conf. Ser.* **2767** 072016

View the article online for updates and enhancements.

You may also like

- Influence of different turbulence models on tip vortex prediction
Mingkun Fang, Na Li, Ran Tao et al.
- Measurement and determination of local film cooling performance along a transonic turbine blade tip with viscous dissipation
Phillip M Ligrani, Hallie Collopy and Ward Manneschmidt
- Active control of the tip vortex: an experimental investigation on the performance characteristics of a model turbine
E Anik, A Abdulrahim, Y Ostovan et al.




This content was downloaded from IP address 154.59.124.113 on 02/07/2024 at 11:00

Journal of Physics: Conference Series **2767** (2024) 072016 doi:10.1088/1742-6596/2767/7/072016

# Experimental study of the impact of blade-tip mounted rotors on the X-Rotor vertical-axis wind turbine

**David Bensason, Andrea Sciacchitano, Carlos Ferreira**

Flow Physics and Technology, Faculty of Aerospace Engineering, Delft University of Technology, Kluyverweg 1, Delft 2629HS, The Netherlands.

E-mail: D.Y.Bensason@tudelft.nl

**Abstract.**

The Horizon 2020 European Commission-funded project - X-ROTOR - proposes a radical rethink of the traditional vertical-axis wind turbine geometry. The X-Rotor vertical axis wind turbine relies on blade-tip mounted rotors, referred to as secondary rotors, for power generation and takeoff. This study examines the aerodynamic effects of secondary rotors on a scaled X-Rotor model's loading in an open-jet wind tunnel. Particle image velocimetry measurements are taken at two cross-stream planes within the volume of rotation of a scaled turbine model at two phase-locked positions. The measurements are compared with cases without secondary rotors present to understand the local impact of the blade-tip mounted devices on the wake and vortex strengths. The results indicate an accelerated turbulent diffusion of the trailing tip-vortex of the X-Rotor, and the subsequent local in-plane velocity gradients induced by the trailing tip-vortex are diminished. These insights and experimental database contribute to the development and validation of numerical models of the X-Rotor with blade-tip mounted rotors.

## 1. Introduction

The X-Rotor [1] is a novel vertical-axis wind turbine concept. The design includes four coned blades connected via a central strut forming an X-shape, coined as the primary rotor, which rotates on its vertical axis. Furthermore, blade-tip-mounted rotors are included on the bottom tips of the blades, which rotate on their horizontal axis and are coined as secondary rotors. The geometry relies on an aerodynamic gearbox concept, where the primary rotor extracts mechanical power from the wind while the secondary rotors are responsible for driving electrical generators. This introduces a theoretical balance between the torque and thrust of the primary and secondary rotors, respectively.

Previous experimental work [2] has explored the primary rotor's near wake, focusing on the complex three-dimensionality resulting from the coned blades to a traditional H-type VAWT geometry. Furthermore, experimental work has explored the impact of wingtip-mounted porous disks on the near wake of an H-type VAWT and demonstrated the aerodynamic gearbox concept [3]. However, experimental studies have yet to be performed on the scaled X-Rotor with rotating secondary rotors.

The present study aims to build on the aforementioned results and fill this research gap by assessing the impact of rotating secondary rotors on the near wake and loading of the

Content from this work may be used under the terms of the Creative Commons Attribution 4.0 licence. Any further distribution of this work must maintain attribution to the author(s) and the title of the work, journal citation and DOI.
Published under licence by IOP Publishing Ltd

X-Rotor. In this work, the flowfield within the volume of rotation of the primary rotor is measured using stereoscopic particle image velocimetry (PIV). This work compares a subset of the measurements to previous results without a secondary rotor [2]. This experimental database will be used to validate and develop numerical models. The remainder of the article is organized as follows: The experimental setup, measurement system, case overview, secondary rotor design, and performance are described in Section 2. An overview of the PIV results and a discussion are given in Section 3. Finally, conclusions and an outlook on future work are provided in Section 4.

## 2. Methodology

### *2.1. Primary rotor model*

An in-house designed and fabricated scaled X-Rotor model (1:100) is used for this experiment, shown in Figure 1. The model consists of four straight blades made of aluminum with a NACA0021 profile and chord of $c = 0.075$m and tip radius of $R_1 = 0.75$m ($D_1 = 1.5$m). The upper and lower blades are 1m and 0.65m long with cone angles of 30° and 50° to the axis of rotation, respectively. The blades are fastened to a rigid crossbeam with a span of 0.50m and the aforementioned profile and chord. The crossbeam is connected to a tower mounted to a frame with instrumentation such as a motor, rotary encoder, torque sensor, and load cells. A detailed overview of the instrumentation is provided by LeBlanc et al. [4]. The rotor is mounted at the center of the test section, shown in Figure 2.

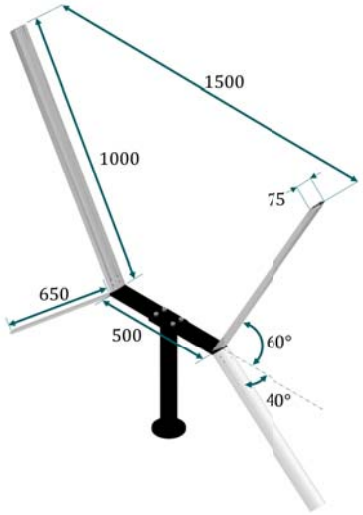


Figure 1: Rendered schematic of the scaled X-Rotor model. All dimensions are in mm.

### *2.2. Wind tunnel*

The experiments are performed in the Open-Jet Facility (OJF) of TU Delft's Aerodynamics Laboratories, as illustrated in Figure 2. The closed-loop tunnel has an octagonal exit section of 2.85m × 2.85m with a contraction ratio 3:1. A constant streamwise velocity of $U_\infty = 4$m/s is used for all measurement cases, and the reported turbulence intensity range is 0.5% - 2% [5].

### *2.3. Secondary rotor design and operating conditions*

The secondary rotors are sized by geometrically scaling the full-scale X-Rotor design [6]. The full-scale design includes a secondary rotor diameter of 9.4m. Given the aforementioned scaling ratio, the lab-scale diameter is 94mm, as shown in Figure 3.

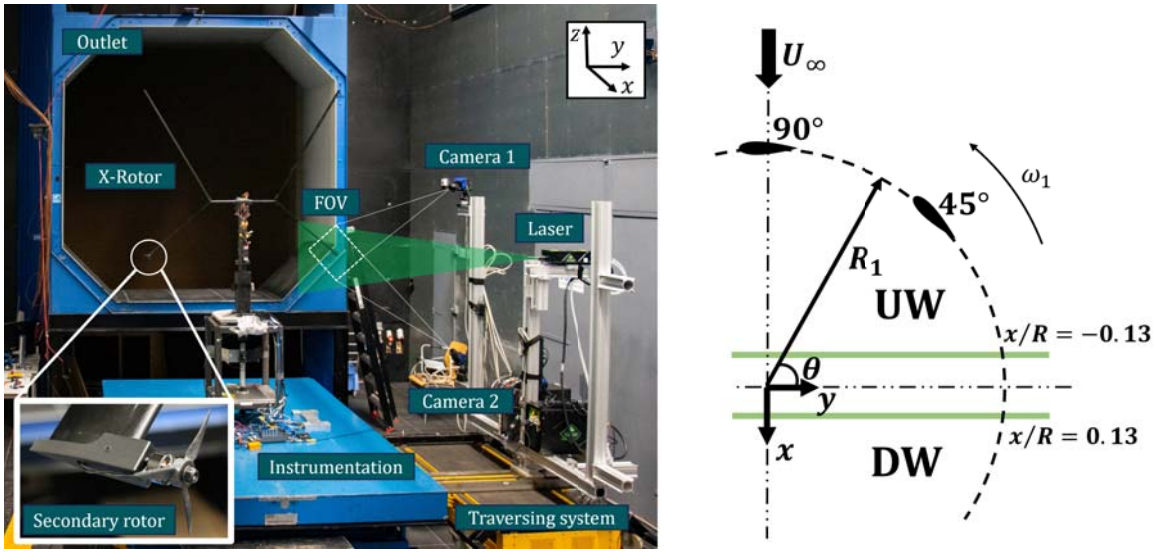


Figure 2: (Left) Experimental setup in the OJF with annotations. (Right) Top-view visualization of the measurement planes (green) along with phase-locked blade positions.

The secondary rotors are mounted to the bottom blade tips of the primary rotor, as visualized in Figure 2. The rotor is made of smoothed 3D-printed PLA and driven by a brushless motor. The motor is mounted to a 3D-printed sleeve of the same material and controlled using an electronic speed controller with governor control mode. The system is powered by a battery and programmed using an Arduino. The batteries and Arduino are mounted in the primary rotor crossbeam and tower, with cables running through the blades to the mounted motor units.

Considering the aerodynamic gearbox concept of the X-Rotor [7], the relationship between the primary rotor power and secondary thrust can be expressed as shown in Equation (1) assuming a 100% conversion efficiency between the extracted power of the primary rotor and the generated power of the secondary rotors.

$$\frac{C_{P1}}{C_{T2}} = n\lambda_1^3 \frac{A_2}{A_1} \tag{1}$$

where $C_{P1}$ and $C_{T2}$ are the power and thrust coefficients of the primary and secondary rotors, respectively. The number of secondary rotors and the tip-speed ratio of the primary rotors are expressed as $n$ and $\lambda_1$, and the ratio between the frontal area of the secondary and primary rotor is expressed as $\frac{A_2}{A_1}$. For this study, the tip-speed ratio of the primary rotor is taken as $\lambda_1 = 4$, yielding a power coefficient of approximately $C_{P1} = 0.4$. The bottom blade tips both house a secondary rotor; thus, $n = 2$. The frontal area of the primary and secondary rotors are $A_1 = 1.29\text{m}^2$ and $A_2 = 0.007\text{m}^2$, respectively. Hence, the desired secondary rotor thrust is calculated as $C_{T2} = 0.58$.

The chord and twist distributions of the secondary rotor are calculated using a backward BEM approach for a constant NACA4412 profile, which uses the geometric constraints, desired thrust coefficient, and tip-speed ratio [1]. This profile was selected given the availability of experimental polars at low Reynolds numbers [8]. The chord and twist distribution of the final design used in this campaign is shown in Figure 4. The thrust as a function of the tip-speed ratio was tested in a wind tunnel, and the results are shown in Figure 4. The data points are fitted using a second-order polynomial curve. Given the aforementioned desired secondary rotor thrust coefficient and fitted curve, the required tip-speed ratio is $\lambda_2 = 4.6$, corresponding to an angular frequency of $\omega_2 = 1566$ rad/s, assuming the blade-tip velocity of the primary rotor of

16m/s.

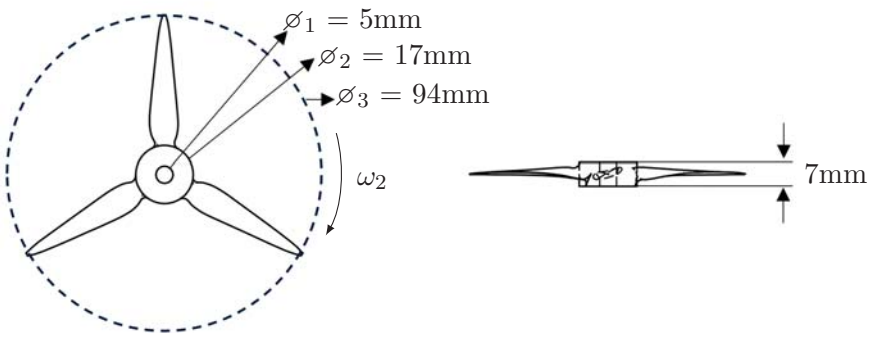


Figure 3: (Left) Front view and (Right) Side view of a schematic of the secondary rotor.

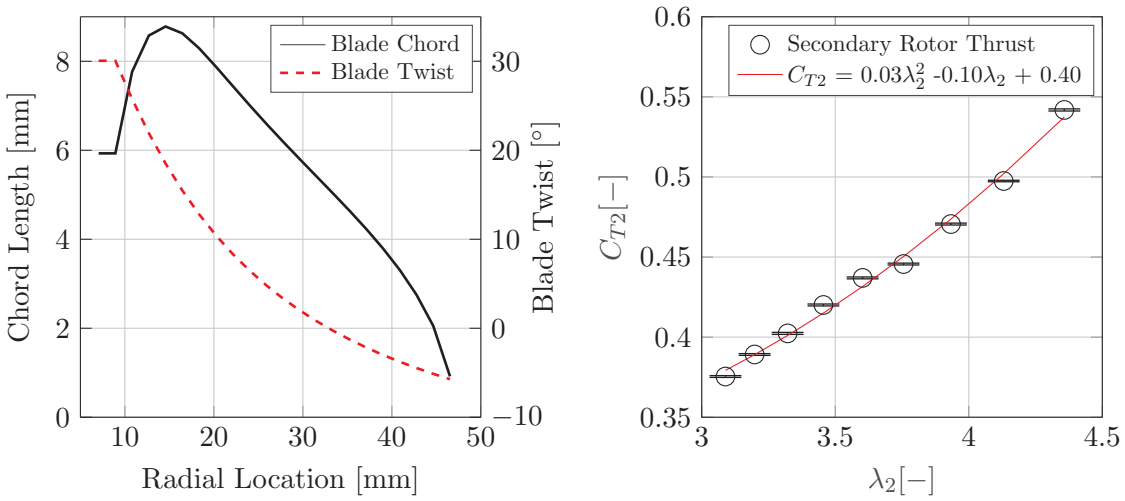


Figure 4: (Left) Secondary rotor chord and twist distribution. (Right) Experimental thrust curve of the secondary rotor as a function of tip-speed ratio. Error bars represent the 95% confidence interval of the estimation of the average value, and the red line shows a second-order fit to the data points.

*2.4. Flow measurement system*

A stereoscopic particle image velocimetry (PIV) setup is used to capture the flowfield at several cross-stream and phase-locked positions of the rotor. An overview of the setup is provided in Figure 2. Seeding is generated using a SAFEX smoke generator with an average particle diameter of 1$\mu$m and particle density $10^3$kgm$^{-3}$. The particles are illuminated via a triggered Quantel Evergreen double-pulsed Nd:YAG laser with a sheet thickness of approximately 4mm and wavelength of 532nm operated at 200 mJ pulse of energy. Images of the illuminated particles are captured via two LaVision's Imager sCMOS cameras. The image resolution of the cameras is 2560px × 2160px and was used with a 105mm lens and numerical aperture of 8. The measurement plane's resulting field of view (FOV) is approximately 50cm × 30cm with an image resolution of 7.16px/mm. A total of 120 images are captured at an acquisition frequency of 15Hz at each FOV. The cameras and laser are rigidly mounted on a traversing system such

that the FOV can be accurately moved and stitched in post-processing in streamwise and lateral directions.

### *2.5. Measurement cases*

The aforementioned measurement system captures the flowfield at several phase-locked positions of the primary rotor and cross-stream locations, as shown in Figure 2. This paper discusses a subset of the plane and phase combinations with overlapping cases with previous work [2]. These are namely $x/R_1$ = -0.13,0.13, where $x/R_1 = y/R_1 = 0$ is taken as the tower's center, at primary rotor phases $\theta = 45°$ and 90°. The flowfield is measured at a constant rotational frequency of the primary rotor of $\omega_1 = 21.3$rad/s, corresponding to a tip-speed ratio $\lambda_1 = \omega_1 R/U_\infty$ of 4, with a chord-based Reynolds number of $\mathrm{Re_c} = \rho \mathrm{U}_\infty \lambda_1 \mathrm{c}/\mu = 8.1{\times}10^4$. The upwind windward (UW) and downwind windward (DW) quadrants are labeled on the schematic, corresponding to primary rotor phase angle ranges $0° < \theta < 90°$ and $270° < \theta < 360°$, respectively.

## 3. Results

### *3.1. Impact on rotor loading*

The change in primary rotor torque $\Delta Q_1$ with and without the secondary rotors present as a function of azimuth over 200 cycles is shown in Figure 5. The primary rotor torque decreases with the presence of the secondary rotors as they add a counter torque to the system. The magnitude of the counter torque added by the secondary rotors $\Delta Q_1$ is 0.98Nm. To validate the thrust operating thrust coefficient of the secondary rotor, the cycle averaged thrust can be approximated using the primary rotor torque difference using Equation (2):

$$C_{T2} = \frac{\Delta Q_1}{0.5 n R_1 \rho U^2 A_2} \tag{2}$$

where $\rho$ is the air density, and $U$ is the flow speed at the blade tip of the primary rotor. This approach assumes that the primary rotor blades produce the same torque with and without the secondary rotors. This is likely untrue, as the interaction of the tip region of the primary rotor blade with the secondary rotor wake will cause a net reduction of the torque of the primary rotor, leading to an overestimation in the calculated secondary rotor thrust. In this case, the cycle averaged flow speed at the blade tip of $U = \lambda_1 \times U_\infty = 16$m/s is used. Hence, the thrust coefficient of the secondary rotor can be approximated to be $C_{T2} = 0.60 \pm 0.12$. This agrees well with the design value described in Section 2.3. We can, therefore, confirm that the machine is operating as we intended and that the aerodynamic gearbox concept is feasible. This design secondary rotor thrust results in a change in the primary rotor power coefficient of $\Delta C_{P1} = 0.41$, consistent with the design case described in Section 2.3.

### *3.2. Velocity fields*

The normalized streamwise flow component is shown in Figure 6 for the cases with and without secondary rotors present. The frontal area of the primary rotor is outlined at a phase of $\theta = 0°$, and the vectors show the in-plane velocity components.

Two distinct flow features are visible in the cases without a secondary rotor: the flow deficits stemming from the trailing vorticity of the blade at azimuth $\theta = 45°$ and 90°, hereinafter referred to as Blade 1, and that from the blade at azimuth $\theta = 225°$, 270°, hereinafter referred to as Blade 2. These trailing vortices are generated at the blade tips and have an azimuthal-dependent strength following Hemholz's theorem due to the cyclically changing load of the primary rotor blades. That of Blade 1 follows the path of the blade, which has just passed the measurement plane and lies close to the frontal area of the rotor as it has had little time to expand. The trailing tip-vortices of Blade 2 leave a large region of flow deficit, which appears more inboard in the frontal area. The in-plane velocity vectors show a presence of local lateral expansion beyond

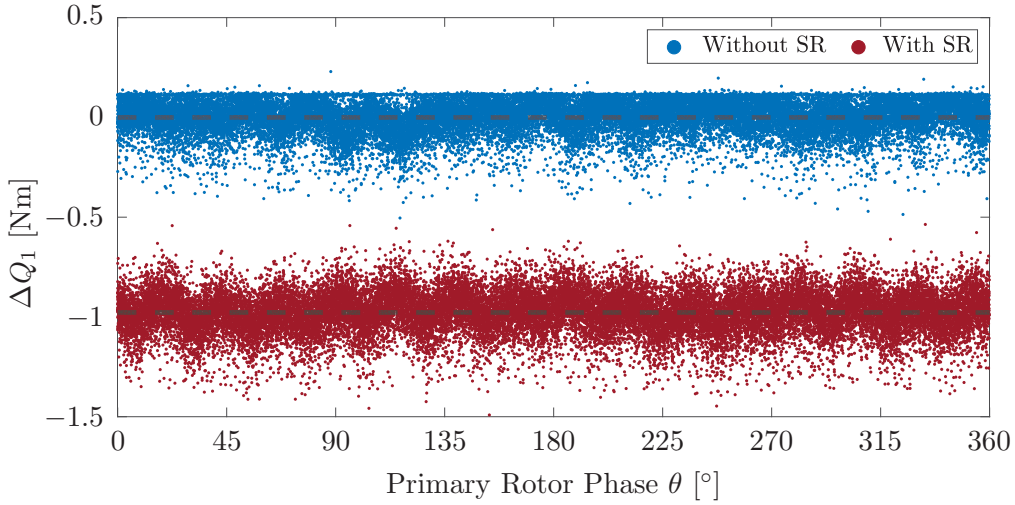


Figure 5: Change in primary rotor torque with respect to the case without secondary rotors (SR) as a function of primary rotor azimuth over 200 cycles. The black dashed lines show the mean change in torque for the respective cases. Note the mean of the case without secondary rotors is zero.

the frontal area of the rotor imposed by the trailing vortex of Blade 1. Similarly, of Blade 2 imposes a significant local upwash and downwash within the volume of rotation of the rotor as the structure convects through the measurement plane.

The wakes behind the secondary rotors along the blade-tip trajectory are clear across all cross-steam planes. At a given primary rotor phase, the flow deficit magnitude increases with the downstream plane, evident by the deeper blue contour. Similar to the case without secondary rotors, the trailing structures of both Blade 1 and Blade 2 are visible in the cross-stream plane and fall within similar vicinities between the two cases. Although the scale of the velocity deficit stemming from Blade 2 is similar, the maximum deficit magnitude appears to be larger in the case without a secondary rotor, suggesting that the secondary rotors induce a higher turbulent diffusion. This seems more evidently true in the wake of Blade 1, where a much weaker local expansion of the wake is visible with the secondary rotors present, highlighted by the smaller in-plane vectors.

### *3.3. Vortex system*

To further understand the cross-stream and in-plane velocities described in Section 3.2, the impact of the secondary rotors on the streamwise vorticity component is analyzed. The normalized streamwise vorticity component for the cases with and without secondary rotors is shown in Figure 7. The frontal area of the primary rotor is shown at a phase $\theta = 0°$ with vectors for the in-plane velocity components.

For the case without secondary rotors, the two coherent vortical structures are visible across all plane and phase combinations. These correspond to the regions of large flow deficit in Figure 6 and are the trailing tip-vortices generated by Blade 1 and Blade 2. The more outboard structure is the tip-vortex generated by the Blade 1, which has just passed the cross-stream plane, whereas the structure inboard (towards the tower) is that generated by Blade 2. At a given cross-stream plane, the vortical structures appear more inboard as the primary rotor blade progresses due to the convection of the curved tip-vortex downstream through the rotation volume. Characteristic of VAWTs, there is a presence of vortex interaction, for example, at a primary rotor phase $\theta =$

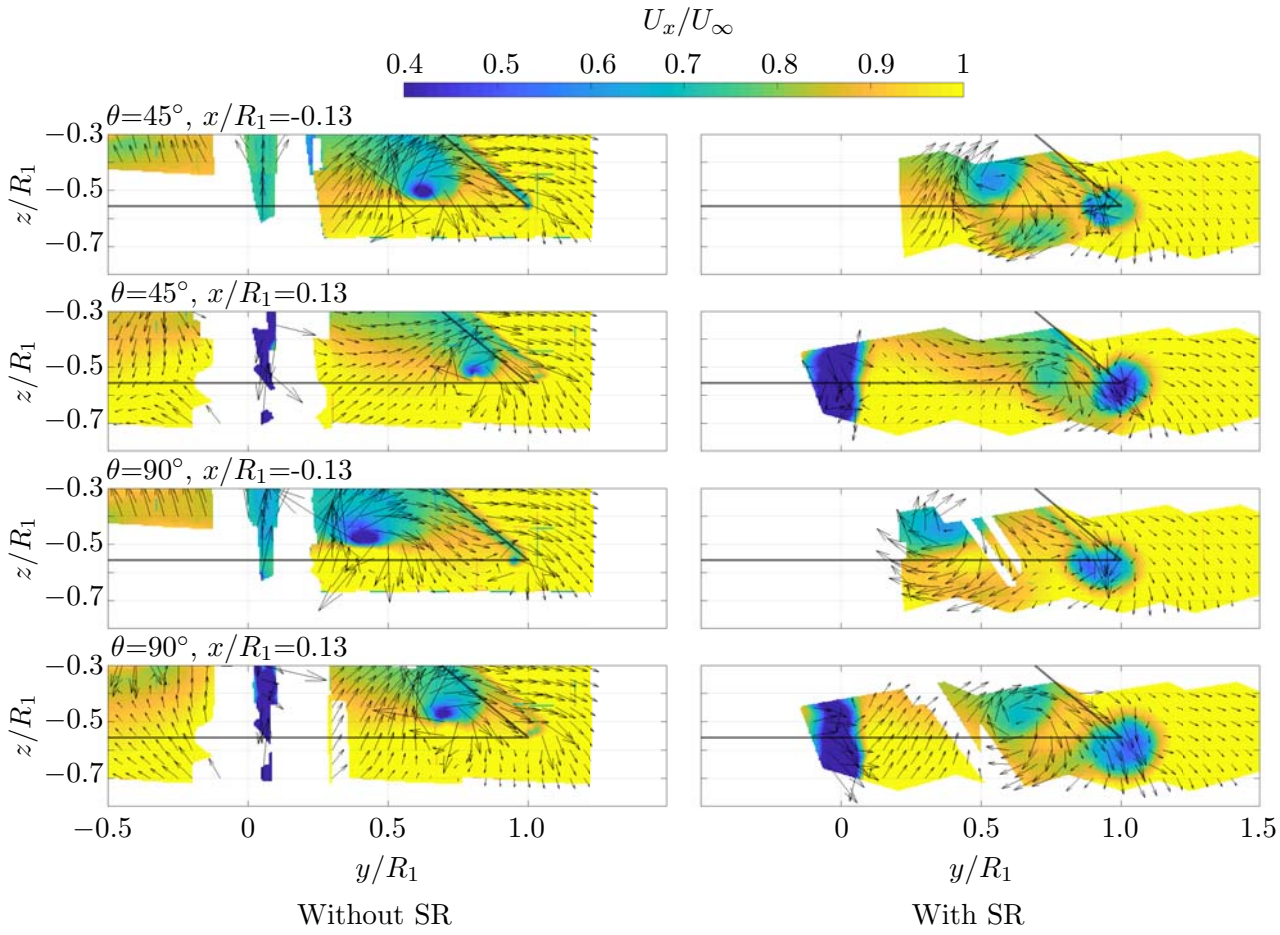


Figure 6: Normalized streamwise velocity $U_x$ at discrete cross-stream and primary rotor phase combinations with and without secondary rotors (SR). Vectors represent the in-plane velocity components. The bottom section of the primary rotor frontal area is shown at a phase of $\theta$=0° with a thin black line.

45° and $x/R_1 = 0.13$, where Blade 1 passes through the shed wake of Blade 2.

Unlike the baseline case, the case with the secondary rotors does not show a coherent tip-vortical structure behind Blade 1 but rather a mix of positive and negative vorticity patches. This is due to the turbulent mixing induced by the secondary rotors, which accelerates the diffusion of the weak primary rotor tip-vortex generated at an early azimuth in the upwind windward quadrant. This more clearly explains the lack of a strong local induction inflicted by coherent vortical structure for the case of Blade 1 with secondary rotors, as discussed in Section 3.2.

Conversely, the vortical structure shed by Blade 2 is more coherent in shape and direction. This is because it is generated at a phase where the primary rotor blade is in a later stage of the upwind windward quadrant, where it produces more load, leading to a stronger and more dominant tip-vortex structure [6]. Hence, the secondary rotors have a relatively smaller impact on the circulation along the primary rotor blade and subsequent vorticity direction. In general, the locations of the vortical structures are similar between the cases with and without secondary rotors, consistent with the regions of flow deficit shown in Figure 6. The size of the

vortical structure of Blade 2 appears larger for the case with secondary rotors, likely due to the accelerated diffusion of the vortex as it interacts with the wake of the secondary rotors.

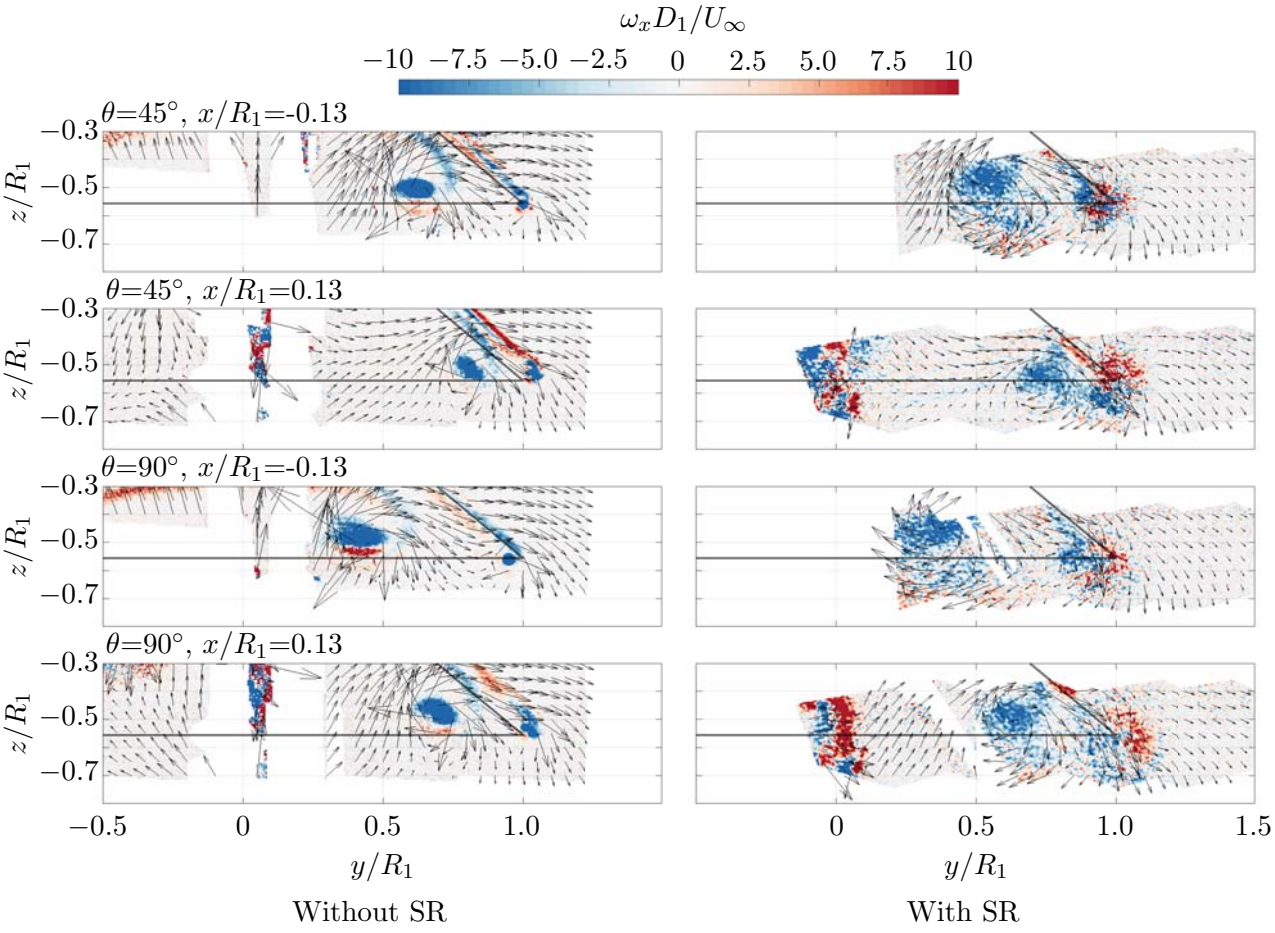


Figure 7: Normalized streamwise vorticity $\omega_x$ at discrete cross-stream and primary rotor phase combinations with and without secondary rotors (SR), where $D = 1.5$m is the tip diameter. Vectors represent the in-plane velocity components. The bottom section of the primary rotor is shown at a phase of $\theta$=0° with a thin black line.

### *3.4. Impact on the circulation*

The flowfields shown in Figure 6 and Figure 7 provide a qualitative understanding of the impact of the secondary rotors on the trailed and shed vortical structures and subsequent wake, highlighting the clear impacts on the shapes and magnitudes with the presence of secondary rotors. To highlight these impacts of the secondary rotors on the blade loads and trailing vortices more concretely, we investigate the circulations of these structures. In theory, the circulation of the vortex trailed by the blade tip should be conserved, assuming the load of the blade is the same with and without the secondary rotors. However, we can expect the integrated load of the blade to be slightly lower with the secondary rotors, as its induction will reduce the perceived velocity around the blade tip and subsequent load.

A comparison of the circulation of these structures is shown in Figure 8. The vortex core centers and outlines are computed by identifying the maximima of $\Gamma_1$ and contour where

$\Gamma_2 = \pi/2$, as introduced by [9]. The circulation is estimated by spatially integrating the vorticity over the vorticity patches defined by the $\Gamma_2$ condition. As discussed in Section 3.3, the vortical structure shed by Blade 1 with the secondary rotors is less coherent. Hence, the sum of the circulations of the dominant vortical structures identified are taken for Blade 1 with secondary rotors. Across all phase and plane combinations for both the cases with and without the secondary rotors, the strength of the vortical structures from Blade 2 is significantly higher. This is because the vortical structures shed by Blade 1 are conceived early in the upwind windward quadrant of the cycle, where the blade loading is relatively low. Those of Blade 2 have had a longer time to convect downstream towards the measurement plane and were conceived later in the upwind windward quadrant, where the blade loading was higher. This can be confirmed further by the fact that at a given cross-stream plane, the circulation of the Blade 2 vortex for both cases increases between phases $\theta = 45°$ and 90°. The same argument can also be made for the case of a fixed phase at different planes. For example, at a phase of $\theta = 45°$, the circulation of the vortex decreases between the upstream and downstream planes. The differences in vortex strength between the cases with and without secondary rotors are minimal for those shed by Blade 2. The largest difference is at the case of $\theta = 90°$ at $x/R_1$ = -0.13. However, this discrepancy can be attributed to the lack of data in the region with secondary rotors due to the optical occlusions of the cameras. The same behaviors in circulation can be observed for Blade 1 of the case without secondary rotors, with a decrease or increase in circulation depending on the point in the quadrant at which the structure was conceived. Except for the outlier case of $\theta = 45°$ at $x/R_1 = 0.13$, the circulation from Blade 1 for the case without is lower than that with secondary rotors, consistent with the discussion in Section 3.3.

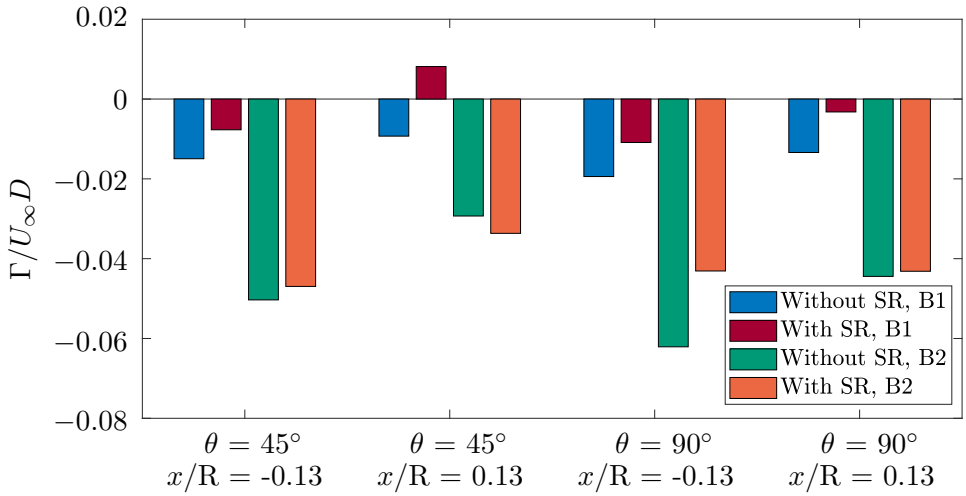


Figure 8: Normalized circulation of the trailing tip-vortices generated by Blade 1 (B1) and Blade 2 (B2) for the cases with and without secondary rotors (SR). The integration area is defined by the contour where $\Gamma_2 = \pi/2$ [9].

## 4. Conclusions

A scaled X-Rotor vertical-axis wind curve with secondary rotors was tested in an open-jet wind tunnel. The results are compared to cases without secondary rotors to shed light on the impact of the devices on the near-wake and primary rotor loading. The main findings can be summarized as follows:

- The thrust of the secondary rotors can be accurately predicted using a simplified cycle average approach of the primary rotor torque. This experimentally demonstrates the balance between the primary rotor torque and secondary rotor thrust, coined the aerodynamic gearbox.
- The secondary rotors create a local wake with an accelerated diffusion of the tip vortex, leading to a decrease in induced in-plane velocity gradients both on the edge and within the volume of rotation of the rotor.
- The strengths of the trailing vortical structures are consistent with the blade loading of the primary rotor as a function of studied azimuth angles. The impact of the secondary rotors on the coherence of the primary rotor tip-vortex is most notable at lower phases of generation, where the primary rotor blade has the lowest circulation, leading to accelerated turbulent diffusion of the tip-vortex structure.

Future work will expand the analysis on an extended set of recorded phase and cross-stream plane combinations with and without secondary rotors. Furthermore, the experimental results will be used to validate numerical models which are being developed.

## 5. Acknowledgments

The authors wish to acknowledge the funding received from the European Union's Horizon 2020 research and innovation program under grant agreement No 101007135.

## References

[1] W. Leithead et al. "The X-rotor offshore wind turbine concept". In: *Journal of Physics: Conference Series*. Vol. 1356. 1. IOP Publishing. 2019, p. 012031.

[2] D. Bensason, A. Sciacchitano, and C. Ferreira. "Near wake of the X-Rotor vertical-axis wind turbine". In: *Journal of Physics: Conference Series*. Vol. 2505. 1. IOP Publishing. 2023, p. 012040.

[3] James Carroll. *D1.3 Periodic Status Report # 2*. Dec. 2022.

[4] B. LeBlanc and C. Ferreira. "Overview and design of pitchvawt: Vertical axis wind turbine with active variable pitch for experimental and numerical comparison". In: *2018 Wind Energy Symposium*. 2018, p. 1243.

[5] LEM Lignarolo et al. "Tip-vortex instability and turbulent mixing in wind-turbine wakes". In: *Journal of Fluid Mechanics* 781 (2015), pp. 467–493.

[6] A. Giri Ajay, D. Bensason, and C. Ferreira. *D2.4 X-Rotor performance and loading evaluation report*. Dec. 2022.

[7] D. Campos-Gaona et al. *Secondary rotors and powertrain design*. Aug. 2022.

[8] K. Koca et al. "Identification of flow phenomena over NACA 4412 wind turbine airfoil at low Reynolds numbers and role of laminar separation bubble on flow evolution". In: *Energy* 144 (2018), pp. 750–764.

[9] L. Graftieaux, M. Michard, and N. Grosjean. "Combining PIV, POD and vortex identification algorithms for the study of unsteady turbulent swirling flows". In: *Measurement Science and technology* 12.9 (2001), p. 1422.